Draft version July 6, 2023
Typeset using LaTeX default style in AASTeX631

Observation of solar radio burst events from Mars orbit with the Shallow Radar instrument

Christopher Gerekos [1] Gregor Steinbrügge [2] Immanuel Christopher Jebaraj [3] Andreas Casillas,[4] Elena Donini,[5] Beatriz Sánchez-Cano [6] Mark Lester [6] Jasmina Magdalenić [7,8] Sean T. Peters [4] Andrew Romero-Wolf [2] and Donald D. Blankenship[1]

[1] University of Texas at Austin Institute for Geophysics, J.J. Pickle Research Campus, 10100 Burnet Road, 78758 Austin, Texas, USA
[2] Jet Propulsion Laboratory, California Institute of Technology, 4800 Oak Grove Drive, CA 91011, USA
[3] Space Research Laboratory, University of Turku, Turku, Finland
[4] Naval Postgraduate School, Monterey, CA, United States
[5] Fondazione Bruno Kessler, Via Sommarive 18, 38123 Povo, Trento, Italy
[6] School of Physics and Astronomy, University of Leicester, University Rd, Leicester LE1 7RH, UK
[7] Center for mathematical Plasma Astrophysics, Department of Mathematics, KU Leuven, Celestijnenlaan 200B, B-3001 Leuven, Belgium
[8] Solar-Terrestrial Centre of Excellence – SIDC, Royal Observatory of Belgium, Avenue Circulaire 3, 1180 Uccle, Belgium

Submitted to ApJ Letters

ABSTRACT

Multispacecraft and multiwavelength observations of solar eruptions such as flares and coronal mass ejections are essential to understand the complex processes behind these events. The study of solar burst events in the radio-frequency spectrum has relied almost exclusively on data from ground-based radiotelescopes and dedicated heliophysics missions such as STEREO or Wind. Reanalysing existing data from the Mars Reconnaissance Orbiter (MRO) Shallow Radar (SHARAD) instrument, a Martian planetary radar sounder, we have detected 38 solar radio burst events with a correlated observation by at least one dedicated solar mission. The very high resolution of the instrument, both in temporal and frequency directions, its bandwidth, and its position in the solar system enable SHARAD to make significant contributions to heliophysics; it could inform on plasma processes on the site of the burst generation and also along the propagation path of associated fast electron beams. In this letter, we characterise the sensitivity of the instrument to type-III solar radio bursts through a statistical analysis of correlated observations, using STEREO and Wind as references. We establish the conditions under which SHARAD can observe solar bursts in terms of acquisition geometry, laying the foundation for its use as a solar radio-observatory. We also present the first analysis of type-III characteristic times at high resolution beyond 1 AU. The scaling laws are also comparable to results found on Earth, except for the fall time; a clearer distinction between fundamental and harmonic components of the bursts may be needed to resolve the discrepancy.

Keywords: Solar burst, type III, radar, Mars

1. INTRODUCTION

The Sun is capable of routinely accelerating electrons to suprathermal energies through eruptive phenomena such as flares, coronal mass ejections (CMEs), and the subsequent shock waves that they drive. These suprathermal electrons emit radiation in the entire electromagnetic spectrum and particularly in the longer radio wavelengths through various mechanisms. Based on the source (streaming electrons, shock waves, etc.) the emission can manifest itself with different morphological properties on the dynamic radio spectrogram. Early observations have distinguished five main spectral types (I–V Kundu 1965), and further sub-classifications have been made since.

Corresponding author: Christopher Gerekos
christopher.gerekos@austin.utexas.edu

In the past two decades, radio frequency observatories onboard heliophysics missions such as the Solar TErrestrial RElations Observatory Ahead & Behind (STEREO A & B/WAVES Bougeret et al. 2008), and Wind/WAVES (Bougeret et al. 1995) have been used to understand various aspects of interplanetary radio emissions. Recently, they have been combined with the Radio Frequency Spectrometer (RFS, part of the FIELDS suite; Bale et al. 2016; Pulupa et al. 2017) onboard the Parker Solar Probe (PSP; Fox et al. 2016) and the radio and plasma waves (RPW; Maksimovic et al. 2020) instrument onboard Solar Orbiter (SolO; Müller et al. 2013) for multi-vantage point studies of hecto-kilometric (H-K) radio emissions (e.g. Jebaraj et al. 2023c; Dresing, N. et al. 2023). While they do not provide the same time-frequency resolution as ground-based instrumentation, observing radio emissions simultaneously from multiple vantage points presents the possibility to investigate the generation and propagation of radio waves (Musset et al. 2021). Previous multi-vantage point observations of solar burst events made beyond 1 AU include (Lecacheux et al. 1989) and (Bonnin et al. 2008).

Planetary radar sounders are a class of spacecraft-mounted remote sensing instruments that operate by recording reflections of electromagnetic waves off a solid planetary body. Such reflections arise when an incoming electromagnetic field encounters a change in the dielectric constant of the medium, such as the space-surface interface, subsurface layering, or subsurface inclusions. The source of this incoming field can be the instrument itself, in which case the radar will transmit a coded waveform (usually a linear chirp) with a power of a few Watts. This mode of operation is known as *active sounding* (Skolnik 1980). Conversely, the incoming field can be a signal of opportunity of astrophysical origin, a recently-proposed mode of operation known as *passive sounding* (Romero-Wolf et al. 2015). Radar sounders typically operate in the deca-hectometre (D-H) wavelength bands.

A particularly successful planetary radar sounder has been the Shallow Radar (SHARAD) instrument (Seu et al. 2004) onboard the National Aeronautics and Space Administration (NASA) Mars Reconnaissance Orbiter (MRO) mission, which was launched towards Mars in 2005 and began observations a year later. SHARAD is sensitive in the 13.3 to 26.7 MHz band, has a time resolution of 1.43 ms before pre-summing, and a frequency resolution of 7.41 kHz (Seu et al. 2004; Croci et al. 2011). The radiating element of SHARAD is a thin-wire 10 m long dipole antenna (Croci et al. 2011). When operating SHARAD, the spacecraft is nominally oriented so that its -Z direction points towards the Martian surface, although some variations in the roll angle have been considered to accommodate unforeseen lobe distribution of the SHARAD antenna pattern (Croci et al. 2011; Campbell et al. 2021). Amongst other discoveries enabled by SHARAD, Grima et al. (2009) characterised the ice purity in the layers of the Martian polar caps, Holt et al. (2008) found evidence of buried glaciers at mid-latitudes, and Campbell et al. (2013a) constrained the roughness and near-surface density of the Martian surface.

In this letter we show how SHARAD can be used to observe solar radio bursts events at unprecedented resolution in the D-H band from space, also marking the first attempt to use a planetary radar sounder as a solar radio-observatory. To this end we devised a purpose-built algorithm for detection of SHARAD-detectable type III bursts in the STEREO/WAVES and Wind/WAVES datasets. We propagated these events in time from the orbits of these spacecraft to the orbit of Mars, and looked up for any instance when the SHARAD receiver was on and when the Sun was not occulted by Mars as seen from MRO. This search for SHARAD type III burst-containing candidates yielded 179 distinct SHARAD radargrams, of which 38 contain solar burst. Through a multivariate statistical analysis of the candidates, we quantify the importance of the acquisition geometry for burst detection. As, by construction, all our SHARAD-detected bursts have at least one correlated observation, we also present comparisons of a few selected bursts observed by SHARAD and the source solar spacecraft, and provide a succinct commentary on their features. Furthermore, we analyse the characteristic times of our dataset of type-III bursts following a methodology close to that of Reid & Kontar (2018) and compare the frequency-dependence scaling laws we obtain with that obtained on Earth and with PSP. We note that Gurnett et al. (2010) mentions having seen solar radio bursts in data from the Mars Advanced Radar for Subsurface and Ionosphere Sounding (MARSIS), another Martian radar sounder (Picardi et al. 2004), but these were treated as parasitic signals, and no attempt was made to study solar radio burst with MARSIS.

This letter is structured as follows. Section 2 presents our methodology for finding correlated observation opportunities and building the proposed list of SHARAD candidates. Section 3 summarises our observations. Section 4 contains in-depth analyses of a few representative SHARAD spectrograms as well as an analysis of the frequency-dependence of the rise and fall time of the type-III bursts in our dataset. Section 5 concludes this letter with a discussion of the proposed dataset and of its perspectives. Appendix A presents a SHARAD duty cycle analysis, Appendix B presents in detail the statistical sensitivity analysis of SHARAD with respect to the geometry of the observations, and Appendix C contains the methodological details of the time-profiles analysis.

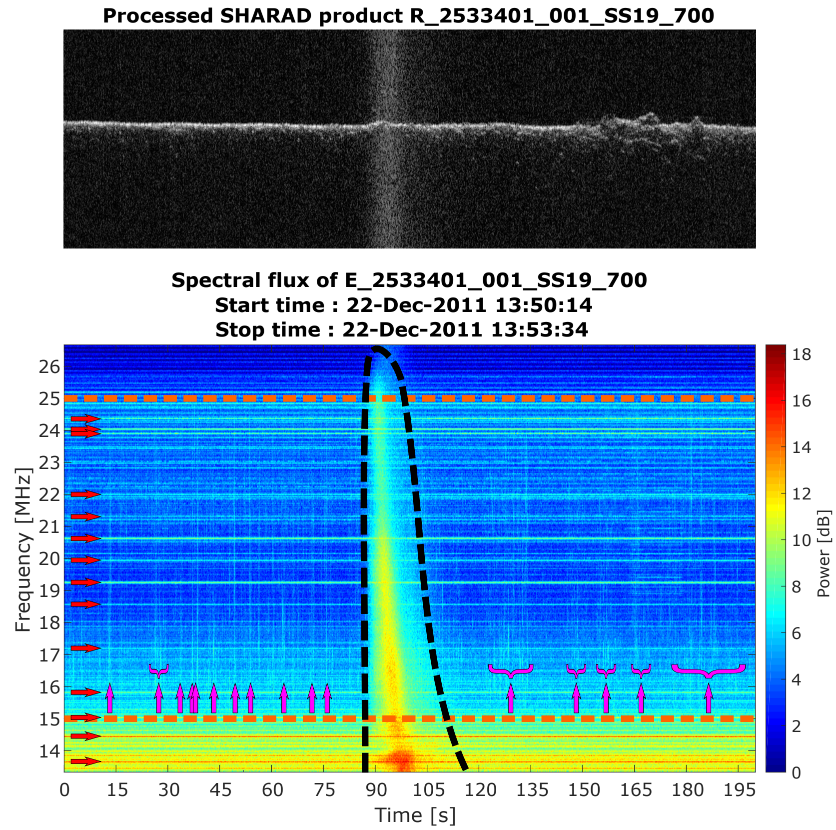

Figure 1. Comparison of processed data product (top) and spectrogram (bottom) for SHARAD product 2533401, along with annotations for the main signals present in the spectrogram. This product contains a type III burst outlined by the dashed black curve ; it is affected by various EMI sources, which are the narrow band signals that are persistent in time and manifest themselves as horizontal traces, the strongest of which are highlighted with horizontal red arrows ; and it contains traces of the reflection of the active chirp, which are are wideband signals with short durations in time and manifest themselves as vertical traces, the strongest of which (or groups of which) are highlighted by vertical purple arrows. The band of flat spectral gain is delimited by the orange dashed lines at 15 and 25 MHz.

2. METHODS AND DATASETS

In this section we present the methodology we used to detect solar radio bursts in STEREO and Wind data and to search for corresponding SHARAD candidates, focusing on type III bursts. The critical parts of the code have been made available along with an accompanying flowchart as Supplementary Material 1 (Gerekos 2023a).

2.1. *Solar radio bursts detection from STEREO and Wind*

We used the the 60 seconds-averaged WAVES products from both STEREO and Wind, covering a period starting on 6 December 2006 (first SHARAD acquisition) and ending on 31 December 2021. An initial screening for bursts is made by integrating the spectrograms over their entire range of frequencies, yielding a one-dimensional time-series of power flux, and by detecting prominences that are one standard deviations higher than the background through the MATLAB proprietary function `findpeaks`. This is done for each 24h-spanning data product. A 3-step fuzzy logic algorithm is then applied on these peaks in order to reject prominences due to interferences or instrument malfunction and to reject genuine type III bursts that do not have significant energy above 13 MHz, about the lowest frequency available to SHARAD. To this end, the algorithm tests peaks flatness, peak asymmetry, and high-frequency content. For more details please refer to (Gerekos 2023a).

Given the large number of type III bursts that these missions recorded, and given the nature of our study, the algorithm is rather restrictive as false positives are more dangerous than false negatives. With this method we detected 5676 bursts with STEREO A, 4340 bursts with STEREO B, and 3538 events with Wind, summing up to a grand total of 13554 events.

2.2. *SHARAD candidate selection*

Each of those events has an associated timestamp t that corresponds to the time of detection of peak power. We propagate this time of detection at the source (STEREO A, B, or Wind) to Martian orbit by considering the radial distance separating the solar spacecraft and Mars at that time. This rests on the hypothesis that the isocontours of burst detection time form circles around the Sun. This radial distance difference is converted into a delay τ assuming propagation at the speed of light in vacuum. In other words, if t' is the supposed time of detection at Mars, we can write

$$t' = t + \tau = t + c^{-1} \left(|\mathbf{v}_M - \mathbf{v}_O| - |\mathbf{v}_w - \mathbf{v}_O| \right) = t + \frac{r_M - r_w}{c}, \tag{1}$$

where $\mathbf{v}_w$, $\mathbf{v}_O$ and $\mathbf{v}_M$ represent the position of the detection source (STEREO A, B, or Wind), the position of the Sun, and the position of Mars, respectively, and where r represents a radial distance from the Sun. These positions can be extracted from the appropriate SPICE kernels. The corresponding Mars detection time t' is computed for all of the 13554 events detected in the previous step. Then, a SHARAD data product is considered a candidate if it satisfies the two following conditions: (i) SHARAD is operating during t'; and (ii) the Sun is not occulted by Mars at t' as seen from MRO. The first criterion is verified by testing that the start and stop time t_1 and t_2 of a given SHARAD data product is such that $t_1 \leq t' \leq t_2$, where t_1 and t_2 are found in the SHARAD product metadata. The second criterion can be easily tested using a SPICE query.

After application of these criteria, we are left with 226 SHARAD detections comprising 179 distinct SHARAD data products (a given event recorded by different solar observatories may correspond to the same SHARAD product). This very strong reduction of the numbers of events, compared with that of Section 2.1 is explained by the very low duty cycle of SHARAD activity (see Appendix A) and by the fact a majority of radar sounding observations were done on the Martian nightside. A complete list of these SHARAD candidates is given as Supplementary Material 2 (Gerekos 2023b).

2.3. *Spectrogram and time-profile generation*

The SHARAD Experimental Data Products (EDR) are real-valued baseband waveforms containing 3600 samples per rangeline (Slavney & Orosei 2007a). A rangeline is a 1D fast-time collection of samples that forms the basic acquisition unit of a radargram. On SHARAD, rangelines are acquired at a frequency of 700 Hz, and have a duration of 135 μs each. The SHARAD dynamic spectrograms shown in this letter are the absolute value of the fast Fourier transform of the EDR product in dB scale. Only the positive-frequency components are displayed (1800 samples). In addition to possible solar radio bursts, these opportunistically-acquired SHARAD spectrograms contain a number of signals of non-solar origin: electromagnetic interference (EMI) and reflections of the active chirp. These are highlighted in Figure 1 for product 2533401, which contains a type III burst. The corresponding processed radargram is also shown for context.

It must be noted that SHARAD has not been calibrated on the ground, meaning there is no formally-generated data products in physical units of spectral flux (Slavney & Orosei 2007b). The gain per frequency band across the whole bandwidth (13.3 to 26.7 MHz) has also not been completely characterised, although it was optimised to be spectrally-flat in the 15 to 25 MHz range (Bernardini et al. 2004). Calibration of SHARAD *a posteriori* is an ongoing effort (Campbell et al. 2021; Castaldo et al. 2013).

No gain de-trending or active chirp removal algorithms have been applied to the spectrograms shown in this work, as our exploitation of the data in this letter remains exploratory. Instead, a basic de-noising using a Gaussian kernel of 3 pixels is applied globally for image rendition concerns. The time-profiles represent a 100-pixel moving average of the raw spectra.

3. OBSERVATIONS

The 179 SHARAD candidates obtained from our search algorithm were visually examined for the presence of solar bursts. Of these candidates, 38 products contain a clear, scientifically-exploitable burst. The list of all candidates, including those without a burst, has been made available as Supplementary Material 2 (Gerekos 2023b) to allow for possible future reanalyses that would look for more subtle signatures, and the subset of SHARAD candidates which contain an unambiguous solar burst is summarised in Table 1. A sensitivity analysis of SHARAD in terms of the relative position and orientation of the instrument, is carried out in Appendix B. We find that, despite the high complexity of the SHARAD antenna pattern, we can predict reasonably well whether a burst detected by STEREO

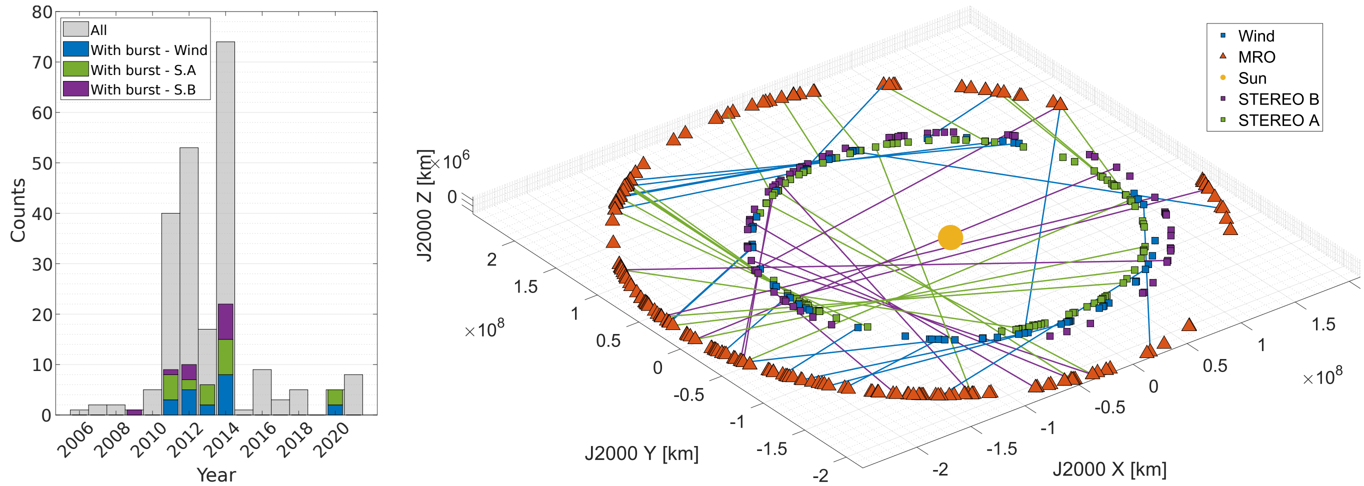

(a) (b)

Figure 2. Visual summary of the generated dataset. (a) Temporal distribution of the SHARAD burst candidates: count of all SHARAD candidates per year in gray, with the burst-containing subsets colour-coded according to the source of the observation. The histogram follows the solar cycle and the proportion of burst-containing products is stable. (b) Spatial distributions of SHARAD burst candidates: positions of MRO, STEREO A, STEREO B, and Wind for all SHARAD candidates. Lines are drawn between the source of the observation and the corresponding SHARAD candidate for every candidate with a burst.

or Wind will be detected by SHARAD: a simple predictive model based on the surveyed acquisition parameters can predict burst show versus no-show with an accuracy of 79.2% (see Figure 5b).

A preview of each of these SHARAD spectrograms is given in Supplementary Material 3 (Gerekos 2023c). Several of these bursts display extensive fine structure (see also Figure 3c), and some bursts have a peculiar dynamic spectra unlike the typical type III profile. Interestingly, a type-II event (SHARAD product 3544101) has also been picked up by our algorithm.

The temporal and spatial distributions of the 226 SHARAD candidate events, with and without burst, is shown in Figure 2. The number of SHARAD candidates throughout the surveyed years closely follows the solar cycle, and the fraction of these candidates that were confirmed to contain a burst stays at around 25% for every year. The additional variability in the number of candidates can be explained by the variation in the yearly SHARAD duty cycle, as shown in Appendix A. This consistency suggests that the geometric selection criteria described in Section 2.2 do not introduce any particular bias. When considering the spatial spread of the observations, it can be observed that the sources of the observations (STEREO A, B, and Wind) are rather evenly distributed whereas the corresponding SHARAD candidates are more concentrated on the negative X-side of the solar system in the J2000 system of coordinates. However, when considering the SHARAD candidates containing a burst, then the distribution of the sources shows a similar unbalance. The first feature is simply explained by the fact a great proportion of bursts were recorded in 2014 and that Mars was in that particular sector during that year, whereas the second observation hints at the angular difference dependence for detectability (see Appendix B): the dedicated solar missions may have been at any place in the solar system during the peak years, but it is those angularly closest to Mars that led to better chances of a SHARAD observation.

4. DISCUSSION

It is well understood that the morphology of the intensity-time profiles of a type III radio burst correspond to the growth of the instability (Voshchepynets et al. 2015; Voshchepynets & Krasnoselskikh 2015; Krasnoselskikh et al. 2019; Tkachenko et al. 2021; Jebaraj et al. 2023b) and the propagation of radio waves (Fokker 1965; Arzner & Magun 1999). The emission, which is a combination of all these processes, is systematically asymmetric in intensity-time profiles (Suzuki & Dulk 1985). Rapid variations in the peak intensity across the observing frequencies is not uncommon in decametre type III bursts (Kontar et al. 2017), and are to be expected when the electron beam evolves in an inhomogeneous medium. These variations may then be used to probe the plasma through which the beam propagates, assuming that the emission is close to the electron plasma frequency.

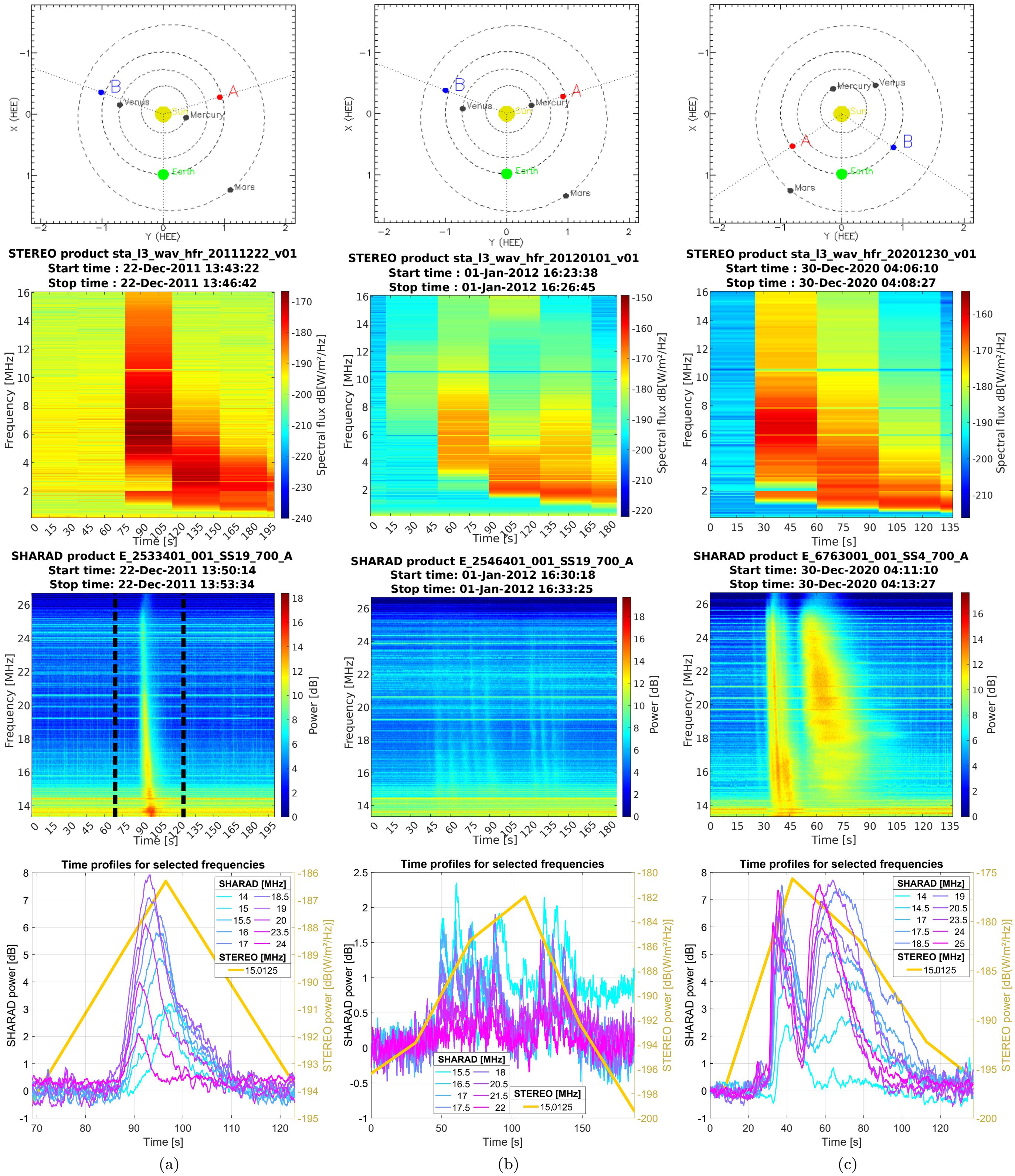

Figure 3. In-depth analysis of three representative elements of the SHARAD burst dataset: (a) SHARAD product 2533401, which is also displayed in Figure 1, (b) SHARAD product 2546401, (c) SHARAD product 6763001. For each case, the top plot represents a map of the solar system. The second row shows the STEREO-captured source burst, in calibrated units. The third row shows the SHARAD spectrogram. The bottom plot contain time-profiles for selected frequencies extracted from the SHARAD spectrogram, along with the 15.0125 MHz line from STEREO for comparison. In the case of 2533401, the dashed black lines on the SHARAD spectrogram show the bounds of the corresponding time-profiles.

Observation Source	SHARAD prod.	Date	ROI start (UT)	ROI stop (UT)	Notes
STEREO B	1301501	06 May 2009	15:46:41	15:47:49	pecul.
STEREO A, B, WIND	2275901	04 Jun 2011	22:03:17	22:05:11	pecul.
STEREO A	2387602	30 Aug 2011	22:35:50	22:41:04	*
STEREO A	2404001	12 Sep 2011	17:29:13	17:30:05	
STEREO A	2433801	05 Oct 2011	23:00:51	23:03:31	
WIND	2532101	21 Dec 2011	13:23:48	13:26:02	
STEREO A, WIND	2533401	22 Dec 2011	13:50:14	13:53:34	*
WIND	2545801	01 Jan 2012	05:28:47	05:31:50	*
STEREO A	2546401	01 Jan 2012	16:30:18	16:33:25	*
STEREO B	2712401	10 May 2012	00:14:07	00:17:09	f.s.
STEREO A, B, WIND	2714201	11 May 2012	09:56:01	09:58:18	
WIND	2746002	05 Jun 2012	05:36:38	05:39:30	
WIND	2760001	16 Jun 2012	03:20:14	03:22:31	*
STEREO B	2792501	11 Jul 2012	09:59:39	10:02:19	
WIND	2813001	27 Jul 2012	10:10:11	10:13:31	*
STEREO A, WIND	3397801	26 Oct 2013	02:49:17	02:51:57	
STEREO A	3401901	29 Oct 2013	07:40:56	07:44:16	
STEREO A	3403202	30 Oct 2013	07:54:43	07:56:14	
STEREO A, WIND	3404001	30 Oct 2013	22:58:27	22:59:47	*
STEREO A, B	3487401	03 Jan 2014	22:21:02	22:23:31	*
STEREO A, B	3537001	11 Feb 2014	13:43:34	13:45:25	pecul.
WIND	3543602	16 Feb 2014	17:41:47	17:43:12	
WIND	3543702	16 Feb 2014	19:25:59	19:34:11	*
WIND	3544101	17 Feb 2014	02:55:44	03:02:24	type-II
STEREO A	3547101	19 Feb 2014	10:49:32	10:52:23	*
STEREO A, B	3564202	04 Mar 2014	18:36:40	18:48:23	
WIND	3582402	18 Mar 2014	22:51:36	22:55:41	
WIND	3617602	15 Apr 2014	09:21:50	09:22:35	f.s.
WIND	3649201	09 May 2014	23:52:30	23:55:22	*
STEREO A, B	3708701	25 Jun 2014	08:42:40	08:44:11	f.s.
STEREO B	3738401	18 Jul 2014	12:37:42	12:39:36	
STEREO A, B	3757101	02 Aug 2014	01:22:51	01:26:06	
STEREO A, B	3766901	09 Aug 2014	16:51:31	16:56:17	*
WIND	3799601	04 Sep 2014	05:03:43	05:04:52	*
WIND	3929701	14 Dec 2014	12:58:33	13:00:39	
STEREO A	6709701	18 Nov 2020	15:40:02	15:42:08	
STEREO A, WIND	6712501	20 Nov 2020	19:37:31	19:38:51	
STEREO A, WIND	6763001	30 Dec 2020	04:11:10	04:13:27	f.s.

Table 1. Table of all the SHARAD candidates where a burst (type III unless otherwise indicated) was identified within the product. The ROI start and stop time refer to the region of interest of the SHARAD spectrograms, and correspond to the temporal bounds of the mosaic shown in Supplementary Material 3 (Gerekos 2023c). In the "Notes" column, "pecul." indicates a possibly different type of burst ; "f.s." signifies a type III burst with extensive frequency-domain fine structure; whereas the asterisk (*) denotes a product that was used in the time-profile analysis of 4.1. See Supplementary Material 2 (Gerekos 2023b) for the candidates where we did not notice a burst.

Figure 3a illustrates a typical type III burst observed on 22 December, 2011. STEREO A/WAVES also detected this burst, albeit at a lower resolution. Figure 3b displays a group of type III bursts observed on 01 January, 2012. Due to limited resolution in the H-K wavelengths, different type III bursts within one are difficult to deconvolve. SHARAD, with its superior capabilities at lower frequencies, reveals nine bursts where STEREO A/WAVES only detects two. Figure 3c presents a type III burst with fine structures called *striae* elements. These bursts can emerge due to electron beam evolution in inhomogeneous plasma, where stronger emissions occur in regions with smaller density inhomogeneities (Jebaraj et al. 2023b). Pulse broadening is mainly due to velocity dispersion of the electron beam exciter (Reid & Ratcliffe 2014), but the Langmuir wave growth can also be hindered in inhomogeneous plasma, resulting in less intense, longer-duration bursts (Voshchepynets et al. 2015; Voshchepynets & Krasnoselskikh 2015). In this example, SHARAD detects three distinct type III bursts, while STEREO A/WAVES observes a single burst without discernible fine structures, underscoring the significance of high time and frequency resolution.

While it is possible to distinguish fine structures and intensity variations using STEREO and Wind observations, their frequency resolution of >4% would mean that only large scale inhomogeneities can be probed (Jebaraj et al. 2023b). On the other hand, SHARAD provides the resolution capable of resolving the fine-scale intensity variations which may then be used in tandem with modern missions such as the Parker Solar Probe during its close encounters. However, a complete characterisation of the spectral gain of SHARAD as well as its sources of EMI is likely to be needed for full exploitation of its spectral resolution.

In this sense, the limitations of SHARAD for heliophysics are of two kinds. The first type of limitation are the instrument-specific limitations that we have just mentioned. Empirically, uneven spectral gain can be addressed by a de-trending of the time-average spectral power for each burst. Regarding EMI, notch filtering has been applied successfully to SHARAD products to enhance the quality of range-compressed observations (Campbell et al. 2021). While these methods are promising for heliophysics-oriented analysis of SHARAD data, one must ensure they do not compromise the natural signals of interest. For this reason, we devolve the study of fine structure within the very high-resolution SHARAD dynamic spectra of type-III bursts to a future study. The second type of limitation arises from using SHARAD opportunistically: the limited number of bursts that we observe in our dataset can be traced to the low duty cycle of SHARAD (see Appendix A), the preference for night-time observations for radar sounding of Mars (Campbell et al. 2013b), and the nadir-pointing geometry favoured for radar sounding of Mars (see Appendix B).

4.1. *Time-profile characteristics*

The very high temporal resolution of SHARAD has the consequence that the fast Gaussian-like rise and the slower exponential decay are effortless to identify, as evidenced by the examples shown in Figure 3. For this reason we propose to study the statistics of the frequency-dependence of the rise time t_r and fall time t_f, computed by fitting an exponentially-modified Gaussian function (Dulk et al. 1984; Reid & Kontar 2018) and by computing the half-widths at half-maximum on either side of the peak intensity (see Appendix C for more details). Reid & Kontar (2018) conducted a comparable study with 31 type-III bursts recorded by LOFAR (Van Haarlem et al. 2013) in the 30 to 80 MHz range. The characteristic times of type-III bursts in the frequency range of 15 to 25 MHz, which provides a natural continuation to (Reid & Kontar 2018), has not been explored beyond 1 AU at the resolutions we have access to here, and constitute a novel result.

We ran our analysis by considering type-III bursts of Table 1 excluding all burst with peculiar morphologies or non-type-III's. In total, 26 type III bursts were analysed. The results for $t_r(f)$, $t_f(f)$, and the derived quantities $t_f(t_r)$ and $(t_f/t_r)(f)$ can be seen in Figure 4, and the best fit power laws for each plot are given in equations 2 through 5, respectively.

$$t_r = \left(44^{+19}_{-13}\right)\left(\frac{f[\text{MHz}]}{1[\text{MHz}]}\right)^{-0.87\pm0.12} \tag{2}$$

$$t_f = \left(26^{+11}_{-7}\right)\left(\frac{f[\text{MHz}]}{1[\text{MHz}]}\right)^{-0.49\pm0.12} \tag{3}$$

$$t_f = \left(2.39^{+0.06}_{-0.05}\right)\left(\frac{t_r[\text{s}]}{1[\text{s}]}\right)^{0.78\pm0.01} \tag{4}$$

$$\frac{t_f}{t_r} = \left(0.61^{+0.14}_{-0.11}\right)\left(\frac{f[\text{MHz}]}{1[\text{MHz}]}\right)^{0.37\pm0.07} \tag{5}$$

A first observation to make is that most bursts taken individually seem to follow a very similar trend as the general fitted law, meaning equations 2 through 5 are representative, and not a product of pure group behaviour.

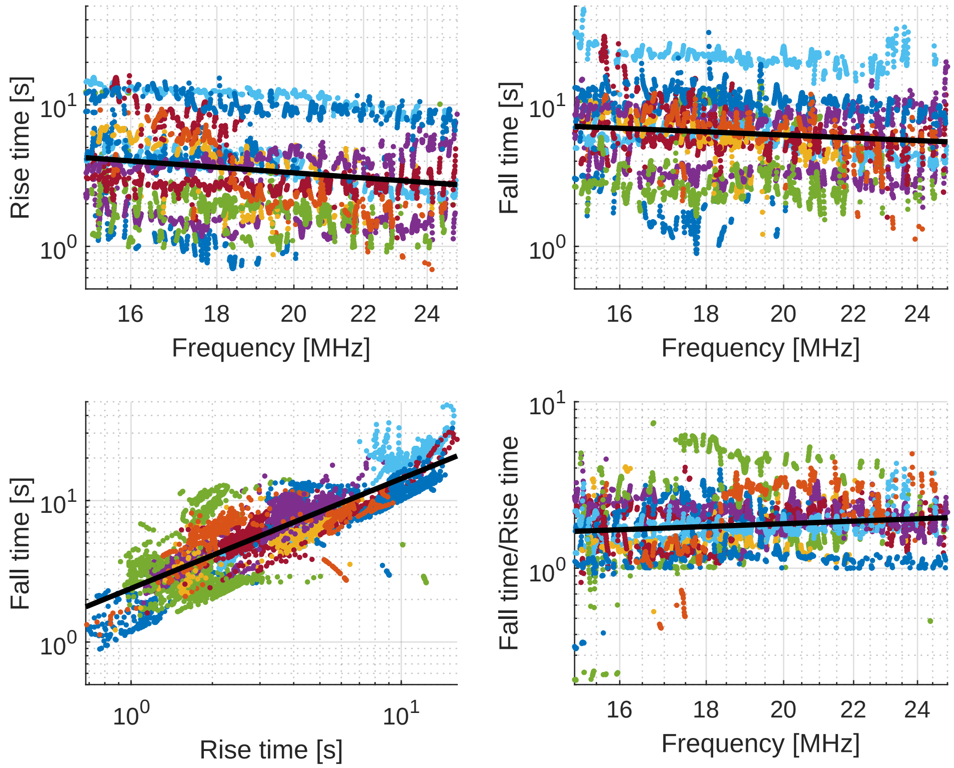

Figure 4. Analysis of rise time and fall time of the suitable type-III bursts recorded by SHARAD after fitting an exponentially-modified Gaussian function onto every frequency line that is unhampered by EMI. The color-coding of the dots represents profiles from an individual burst, with some colours being reused. The black line is the best power-law fit, the equations for which is given in formulae 2 through 5. See Appendix C for methodology.

The rise time exponent -0.87 ± 0.12 is very close to that of Reid & Kontar (2018), who found -0.77 ± 0.14. Interestingly, SHARAD data for the fall time indicates an exponent of -0.49 ± 0.12 and differs rather substantially from the LOFAR measurement of -0.89 ± 0.15. The rise time is closely linked to the exciter function, *i.e.* the growth of Langmuir waves and inherits its characteristics (Krasnoselskikh et al. 2019), and it is thus expected to behave similarly at different points of the solar system for a given frequency. *Stricto sensu*, it is the decay time, measured as the rate of the exponential decay of the burst, that best encapsulates the effects of propagation and scattering (Krupar et al. 2020), rather than the fall time computed here as the second half-width at half-maximum. Nevertheless, in the case of fundamental emissions, the fall time is not completely immune to propagation effects, and can be thought as a convolution between the characteristics of the source and the electromagnetic wave propagation effects (Reid & Kontar 2018) ; it is therefore not excluded that the discrepancy we observe for the fall time at 1.5 AU is partly due to such effects. On the other hand, it is widely understood that these effects are minimal for higher harmonics (Melrose 1980). Interestingly, the fall time frequency-dependence matches very well with that derived from PSP observation, but only for the harmonic component of the bursts Jebaraj et al. (2023a). We did not differentiate between fundamental and harmonic components in this study, so we cannot exclude some kind of selection bias towards the former, either. In this case, our results would indicate very little propagation and scattering effects up to 1.5 AU, but the rise time we obtained is substantially different from that of Jebaraj et al. (2023a) for harmonic emissions (-0.46 ± 0.08). A thorough investigation of the fundamental vs. harmonic content of our SHARAD-detected burst dataset as well as the derivation of their exponential decay scaling law is needed to fully elucidate the issue. We defer this to a future study.

Computing the fall time as a function of the rise time, we find that the former is always longer than the latter, as expected, outliers notwithstanding. The ratio of the two measures the burst asymmetry as a function of frequency, where we observe a weak positive dependence. With a ratio of 1.1 at 25 MHz, our results are almost a direct low-frequency continuation of those of Reid & Kontar (2018).

5. CONCLUSIONS AND OUTLOOK

In this letter, we demonstrated that planetary radar sounders such as SHARAD can be used as high-resolution solar radio-observatories, we presented a quantitative analysis of the sensitivity of SHARAD to solar burst events based on the statistics of correlated observations from a geometric standpoint, and extracted the characteristic times of type-III bursts from this dataset.

The characteristic times analysis at 1.5 AU revealed a behaviour that is overall consistent with Earth-acquired data, but the frequency-dependence of fall time depicted a more complex picture. We found that it scales flatter compared to the recent metric observations by Reid & Kontar (2018) and similar to the scaling laws obtained by Jebaraj et al. (2023a) for second harmonic components. These scaling laws suggest that the evolution of the beam-plasma system in the decametre wavelengths plays a crucial role: if our dataset contains mostly fundamentals, the deviation from Reid & Kontar (2018) would imply that propagation effects do not influence the fall time, which is then primarily determined by the characteristics of the Langmuir wave spectrum. To draw a more general conclusion, discriminating between fundamental and harmonic emissions is crucial, as it is generally expected that the second harmonic is not significantly affected by propagation effects, and bursts characteristics at 1 and 1.5 AU remain consistent with observations near the Sun.

Our findings show that SHARAD observations can bring the large advancements in the understanding of the generation and propagation of the radio bursts at the distances even as far as the Mars orbit. In addition to studying characteristic times at 1.5 AU, the capabilities of SHARAD could be leveraged to study fine-structure, provide additional points of observation in burst triangulation, and its bandwidth completes the spectrum between typical dedicated solar missions and earth radiotelescopes. From the perspective of radar science, correlated observations with STEREO can also help the absolute calibration of SHARAD. Since all bursts are identifiable one-to-one between the two datasets, comparison between the absolute power flux recorded at STEREO with the dBs above background recorded at SHARAD allows its calibration.

It must be noted that the catalogue of type III bursts we present is limited to correlated observations only. There are likely more bursts within the SHARAD archive that could be found through direct inspection. For example, a survey of the MARSIS dataset (in which solar radio bursts have also been seen) is planned amongst future work in order to produce a complete catalogue of MARSIS solar radio burst observations, which will be compared with SHARAD to get a fuller frequency spectrum of the co-observed bursts. The main limitation of using radar sounder data of the Sun is the fact they typically operate no more than a few minutes or tens of minutes a day, and cannot function as a round-the-clock survey instrument.

The results presented here can also be used for future planetary missions. In this decade, two missions carrying radar sounder instruments will be launched towards the Jupiter system (Blankenship et al. 2009; Bruzzone et al. 2011) as well as one towards Venus (Bruzzone et al. 2020), and these instruments too could be utilised for solar radio-frequency observations.

6. ACKNOWLEDGEMENTS

This work was supported by the G. Unger Vetlesen Foundation and by JPL's Innovative Spontaneous Concepts in Research and Technology Development program. Part of this research was carried out at the Jet Propulsion Laboratory, California Institute of Technology, under a contract with the National Aeronautics and Space Administration. I.C.J. is grateful for support by the Academy of Finland (SHOCKSEE, grant No. 346902). B.S.-C. acknowledges support through STFC Ernest Rutherford Fellowship ST/V004115/1. M.L. acknowledges support through STFC grant ST/W00089X/1. J.M. acknowledges funding by the BRAIN-be project SWiM (Solar Wind Modeling with EUHFORIA for the new heliospheric missions). The authors wish to express their gratitude to Bruce Campbell, Dirk Plettemeier, Marco Mastrogiuseppe, Vratislav Krupar, Marc Pulupa, Vladimir Krasnoselskikh, and Milan Maksimovic for the excellent discussions.

APPENDIX

A. SHARAD DUTY CYCLE ANALYSIS

To provide additional context on the discussion of the general properties of the dataset (Section 3) and to highlight the targetted nature of the instrument (as opposed to a survey instrument such as WAVES), we present a brief analysis of the activity duty cycle of SHARAD over the years. Starting from the SHARAD EDR label files, we extracted the radargram start time and stop time for each radargram in the entire SHARAD dataset in the period of study (6 December 2006 to 31 December 2021) in order to compute the duration of that radargram. Taking the cumulative sum of all these durations for each year, we obtain the durations shown in Table 2. On an average year, SHARAD will have been on for about a million seconds, corresponding to a duty cycle of about 3%. Aside from the solar cycle, part of the variability of the number of candidates counted in Figure 2a can be traced to the fraction of the time SHARAD was operating (for instance, the dip in candidates in 2013).

Year	2006*	2007	2008	2009	2010	2011	2012	2013	2014	2015	2016	2017	2018	2019	2020	2021
Activity [10^6 s]	0.05	1.01	1.14	0.48	1.06	0.84	1.35	0.68	1.50	0.42	1.08	0.60	1.08	0.77	1.74	1.07
Duty cycle [%]	0.15	3.48	3.60	1.51	3.36	2.67	4.28	2.17	4.74	1.32	3.43	1.91	3.43	2.44	5.51	3.39

Table 2. SHARAD operating time throughout the surveyed years, expressed in number of seconds per year (activity) and in percentage over a given year (duty cycle). The asterisk * denotes a partial year.

B. SHARAD SENSITIVITY TO TYPE III BURSTS

Of the 179 SHARAD candidates picked up by the algorithm described in Section 2, 38 contain a prominent burst, a fraction of 21.23%, and 141 were identified as not containing a burst. In this appendix we shall discuss these figures and quantify the effects of several geometrical factors on this cross-detection rate.

It would be difficult to compute an overall probability of detection of solar bursts with SHARAD, given that SHARAD-detectable bursts must obey rather stringent conditions of frequency content, but as the vast majority of SHARAD data is uncorrupted, it can be assumed to be very low. In that regard, a "success rate" of 21.23% is a comparatively high figure.

One of the most important parameters that influences the detection of solar radio bursts with SHARAD should be the absolute power of the burst as detected by the source of observations (STEREO A, B, or Wind). However, it is not a parameter we can uniformly analyse, Wind/WAVES data has not yet been formally calibrated and issues of cross-calibration of STEREO/WAVES and Wind/WAVES are still being debated (Krupar, pers. comm., 2022). Parameters of geometrical nature, however, can be analysed uniformly. The non-isotropic nature of type III bursts (Musset et al. 2021) is expected to lead to a preferential detection if the angle between the source spacecraft and MRO with respect to the Sun (marked as ϕ in Figure 5a) is small. It is also expected that the orientation of MRO plays a major role in the detectability of bursts due to the antenna pattern of SHARAD (Croci et al. 2007). In processed radar sounding data, variations of gain of up to 4 dB have been observed by Campbell et al. (2021). The position of the high-gain antenna (HGA) and the orientation of the solar panels of MRO are also known to considerably affect the antenna pattern of SHARAD (Campbell et al. 2021). Due to the complexity and interdependence of these effects, however, we chose to focus on the orientation of the antenna only.

Since the orientation towards the Sun is the most relevant parameter, we shall define pitch, yaw, and roll angles with respect to that direction as follows. We first define a set of three reference unit vectors:

$$\hat{\mathbf{v}}_1 = \frac{\mathbf{v}_O - \mathbf{v}_{MRO}}{|\mathbf{v}_O - \mathbf{v}_{MRO}|}, \tag{B1}$$

$$\hat{\mathbf{v}}_2 = \hat{\mathbf{v}}_{\mathrm{z,ECLIPJ2000}}, \tag{B2}$$

$$\hat{\mathbf{v}}_3 = \frac{\hat{\mathbf{v}}_1 \times \hat{\mathbf{v}}_2}{|\hat{\mathbf{v}}_1 \times \hat{\mathbf{v}}_2|}, \tag{B3}$$

where $\mathbf{v}_O = (0,0,0)$ is the position of the Sun in the J2000 system of coordinates, and $\mathbf{v}_{MRO}$ that of MRO. By construction, $\hat{\mathbf{v}}_1$ always points from MRO towards the Sun. $\hat{\mathbf{v}}_2$ is the normal to the ecliptic plane, and $\hat{\mathbf{v}}_3$ completes the orthonormal basis. With these vectors, we define the following projections of the $\hat{\mathbf{u}}_{j,MRO}$, $(j = x, y, z)$ vectors, which form the basis of MRO-fixed orthonormal unit vectors (Croci et al. 2007):

$$\mathbf{w}_x = \hat{\mathbf{u}}_{x,MRO} - (\hat{\mathbf{u}}_{x,MRO} \cdot \hat{\mathbf{v}}_3)\hat{\mathbf{v}}_3, \tag{B4}$$

$$\mathbf{w}'_x = \hat{\mathbf{u}}_{x,MRO} - (\hat{\mathbf{u}}_{x,MRO} \cdot \hat{\mathbf{v}}_2)\hat{\mathbf{v}}_2, \tag{B5}$$

$$\mathbf{w}_z = \hat{\mathbf{u}}_{z,MRO} - (\hat{\mathbf{u}}_{z,MRO} \cdot \hat{\mathbf{v}}_3)\hat{\mathbf{v}}_3. \tag{B6}$$

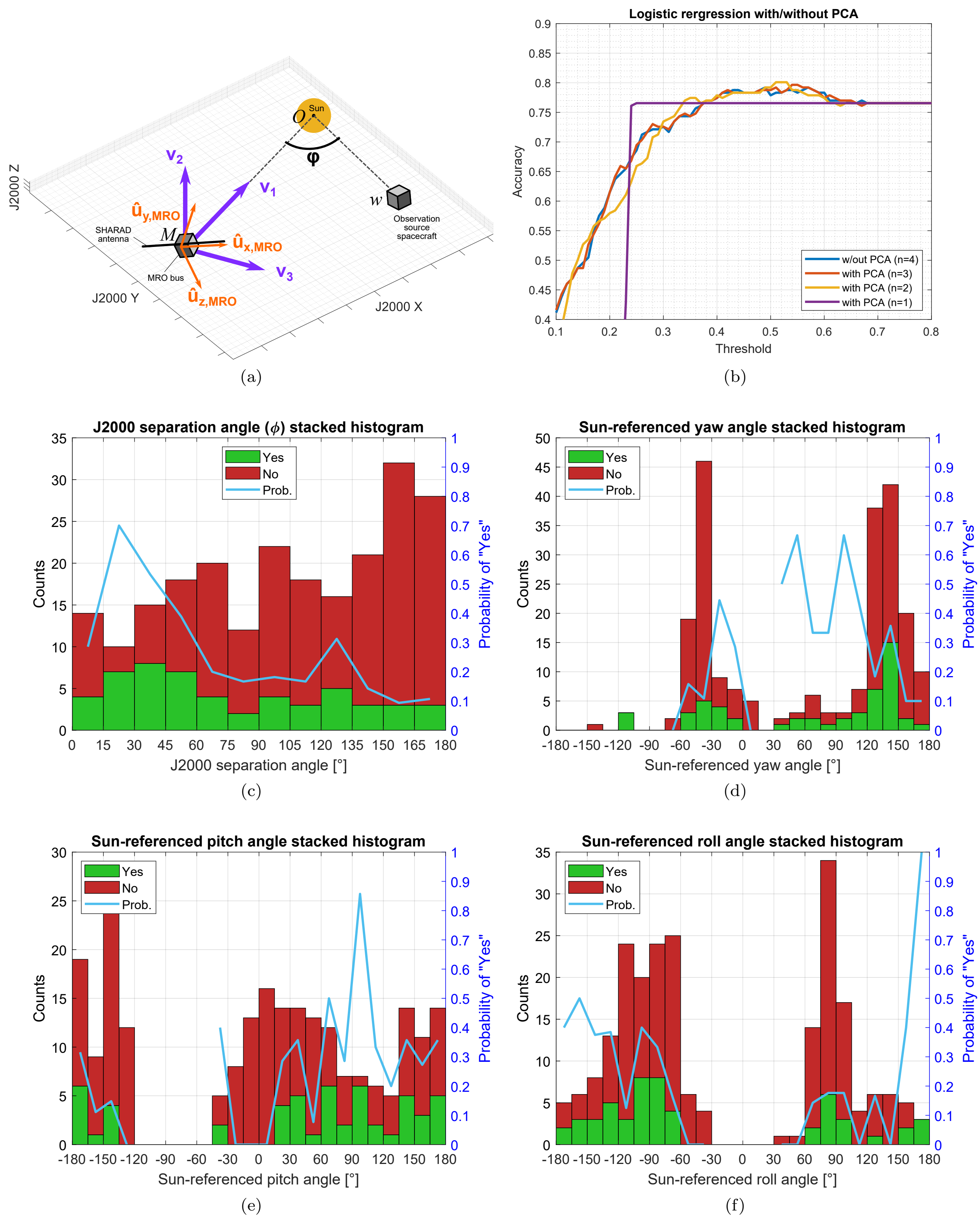

Figure 5. Sensitivity of SHARAD to geometrical acquisition parameters. (a) Illustration of several key quantities in the definition of relevant angles. (b) Multivariate logistic regression using the feature vectors generated by the principal component analysis. (c)-(f) Histograms of the number of burst detection ("Yes") burst no-detection ("No") and the probability of detection (ratio of "Yes" to "Yes" + "No") for J2000 separation, yaw, pitch, and roll angles, respectively.

In Figure 5a, the vectors $\hat{\mathbf{v}}_i$, $(i = 1, 2, 3)$ and $\hat{\mathbf{u}}_{j,MRO}$, $(j = x, y, z)$ are represented in purple and orange, respectively. $\mathbf{w}_x$ is the projection of $\hat{\mathbf{u}}_{x,MRO}$ onto the $(M, \hat{\mathbf{v}}_1, \hat{\mathbf{v}}_2)$ plane, $\mathbf{w}'_x$ is the projection of $\hat{\mathbf{u}}_{x,MRO}$ onto the $(M, \hat{\mathbf{v}}_1, \hat{\mathbf{v}}_3)$ plane, and $\mathbf{w}_z$ is the projection of $\hat{\mathbf{u}}_{z,MRO}$ onto the $(M, \hat{\mathbf{v}}_1, \hat{\mathbf{v}}_2)$ plane.

These constructions allow us to define the desired Sun-based pitch, yaw, and roll angles as follows:

$$\text{Yaw} = \text{sgn}(\hat{\mathbf{w}}'_x \cdot \hat{\mathbf{v}}_3) \arccos(\hat{\mathbf{w}}'_x \cdot \hat{\mathbf{v}}_1) \tag{B7}$$

$$\text{Pitch} = \text{sgn}(\hat{\mathbf{w}}_x \cdot \hat{\mathbf{v}}_2) \arccos(\hat{\mathbf{w}}_x \cdot \hat{\mathbf{v}}_1) \tag{B8}$$

$$\text{Roll} = \text{sgn}(\hat{\mathbf{w}}_z \cdot \hat{\mathbf{v}}_2) \arccos(\hat{\mathbf{w}}_z \cdot \hat{\mathbf{v}}_1) \tag{B9}$$

where sgn(·) is the sign function. A 0° value for both yaw and pitch has the antenna axis pointed towards the Sun (*i.e.* zero gain for an ideal dipole). The roll angle controls the position of SHARAD with respect to the Sun and the MRO bus (the gain of an ideal dipole is agnostic to roll).

We have made two types of statistical analysis based on these four angles (i.e., source separation angle, MRO pitch, MRO yaw, MRO roll): (i) a principal component analysis (PCA), and (ii) histograms and probability of detection for each angle independently. The results can be seen in Figure 5b and 5c-f, respectively.

Regarding the components of the PCA (which are orthogonalised linear combinations of the four angles), the first three contained 96.45% of all variability in the original data, the first two 73.41%, and the first component only 47.13% of all variability. The correlations between any pair of angles is weak (< 0.2) except for yaw and roll, which are strongly anti-correlated (-0.8), a result of the attitude control on MRO, itself on a polar orbit **?**. We also performed a multivariate logistic regression using these PCA feature vectors to classify the bursts as "Yes" or "No", based on a selectable threshold to convert the continuous output of the predictive model in the $[0, 1]$ range to a "Yes"/"No" binary. This predictive model has a classification accuracy peaking at 0.792 for a threshold of 0.49 (a very sensible threshold for the purpose) using all four feature vectors.

From the J2000 separation angle histogram, it is clear that detection is preferentially successful at low angles, with a probability of cross-detection reaching 0.7 when the angle between MRO and the source of observation is around 20°. Regarding orientation, the probability of detection peaks when pitch and yaw are both close to 90°. These angles put the radar axis perpendicular to the Sun (the former, horizontally, and the latter, vertically), which is the configuration for which maximal gain is expected. The absence of observations for some ranges of angles can be traced to MRO orbit specifics coupled with the no-occultation condition we imposed on the candidates. Probability of detection also peaks when the roll angle approaches ±180°, that is, when $\hat{\mathbf{u}}_{z,MRO}$ is aligned but opposite to $\hat{\mathbf{v}}_1$ (see Figure 5a). For favourable yaw and pitch, such roll angles place SHARAD "in front" of the Sun, with the bus and the other large structures "behind" it. Intuitively, this is also a configuration that is expected to maximise the SHARAD gain, as it approaches that of traditional radar sounding (Campbell et al. 2021).

C. TIME-PROFILE ANALYSIS METHODOLOGY

The time-profile analysis was run on all the "canonical" type-III bursts detected by SHARAD, that is, all those listed in Table 1 with an asterisk in the "Notes" column. This excludes those with peculiar morphologies (*e.g.* 2712401), those with extensive fine-structure (*e.g.* 3617602), and those which are not type-III's (*e.g.* 3544101). A similar sieving was done in Reid & Kontar (2018). When a given SHARAD data product contained several bursts, all those that are exploitable within this product were included. This left 26 individual bursts to analyse. Of these bursts, all frequency lines containing EMI were removed. For a given product, the EMI lines were identified through a global time-average of the dynamic spectrum, the application of a median filter with kernel size 101, and the detection of all frequency lines that were above this trendline. We also exclude the frequency lines at the edges of the instrument's capabilities, and ran our analysis in the 15 − 25 MHz range, the bandwidth the instrument was optimised for. After exclusion of EMI and edge frequencies, about 800 frequency lines per burst (out of 1800) are still available for time-profile analysis. In total, we thus analysed about 25 000 profiles.

The five-parameter function that was used to fit all these bursts is the exponentially-modified Gaussian function, given by:

$$g(a, b, \mu, \sigma, \lambda; x) = a\frac{\lambda}{2}\exp\left\{\frac{\lambda}{2}\left(2\mu + \lambda\sigma^2 - 2x\right)\right\}\left(1 - \text{erf}\left\{\frac{\mu + \lambda\sigma^2 - x}{\sqrt{2}\sigma}\right\}\right) + b, \tag{C10}$$

where a controls the overall scaling of the burst, and b, its floor; μ is the mean of the Gaussian sector of the function, and σ^2, its variance; lastly, λ controls the decay rate of the exponential sector. The error function is defined as

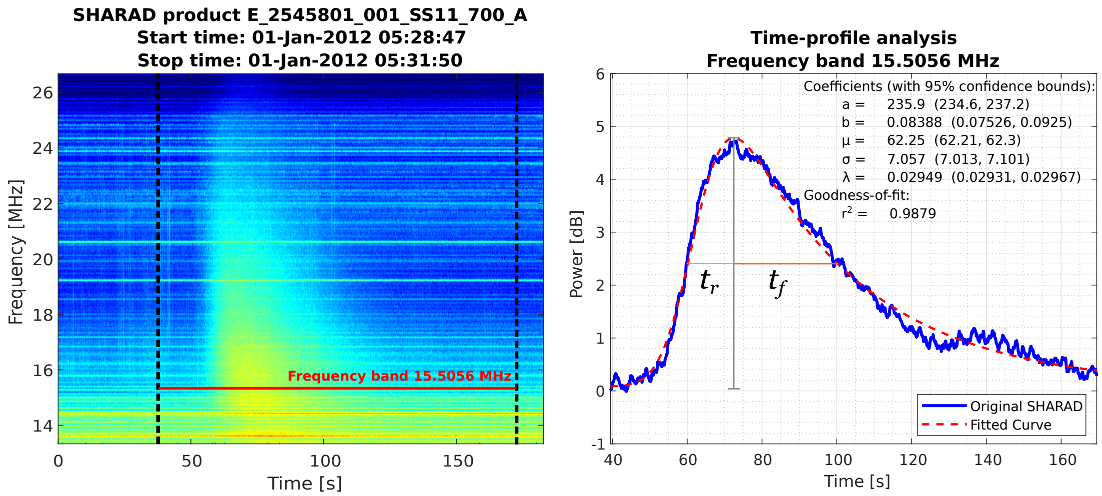

Figure 6. Worked-out example of a time-profile extraction and fit on SHARAD product 2545801 using the EMI-free frequency band of 15.5056 MHz. The black vertical dashed lines on the dynamic spectrum represent the portion of the product that was fed into the fitting subroutine. The coefficients displayed next to the fitted curve correspond directly to those of equation C10. The rising and fall times t_r and t_f were derived as the first and second half-width at half-maximum, itself computed as the difference between the maximum of the curve and the floor parameter b.

$\mathrm{erf}(z) \equiv 2(\pi)^{-1/2} \int_0^z e^{-t^2} \mathrm{d}t$. The rise time t_r and fall time t_f are then computed as the two half-widths at half-maximums of the fitted curve. In Figure 6 we show an example of a SHARAD profile along with its fitted function, and a graphical representation of t_r and t_f.

Along with the quantities of interest, we also recorded the r^2 coefficient for each fit, in order to exclude fits of bad quality when compiling the data shown in Section 4.1. Bad fits can occur when the signal-to-noise ratio of the burst is very low, when several closely-spaced bursts forces us to constrain the cropping around each of them, or when the profile is contaminated by reflections of the active SHARAD chirp. Due to the abundance of data points, we were able to apply very strict fit quality criteria, considering only the profiles for which $r^2 > 0.95$, and still be left with about 7000 data points in the plots of Figure 4.

REFERENCES

Arzner, K., & Magun, A. 1999, Astronomy and Astrophysics, 351, 1165

Bale, S. D., Goetz, K., Harvey, P. R., et al. 2016, SSRv, 204, 49, doi: 10.1007/s11214-016-0244-5

Bernardini, F., Croci, R., Fois, F., et al. 2004, Alenia Spazio S.p.A., Doc. No. MAN-SHR-0007-ALS

Blankenship, D. D., Young, D. A., Moore, W. B., & Moore, J. C. 2009, Europa. University of Arizona Press, Tucson, AZ

Bonnin, X., Hoang, S., & Maksimovic, M. 2008, Astronomy & Astrophysics, 489, 419

Bougeret, J.-L., Kaiser, M. L., Kellogg, P. J., et al. 1995, Space Science Reviews, 71, 231

Bougeret, J. L., Goetz, K., Kaiser, M. L., et al. 2008, SSRv, 136, 487, doi: 10.1007/s11214-007-9298-8

Bruzzone, L., Alberti, G., Catallo, C., et al. 2011, Proceedings of the IEEE, 99, 837, doi: 10.1109/JPROC.2011.2108990

Bruzzone, L., Bovolo, F., Thakur, S., et al. 2020, in IGARSS 2020-2020 IEEE International Geoscience and Remote Sensing Symposium, IEEE, 5960–5963

Campbell, B. A., Morgan, G. A., Bernardini, F., et al. 2021, Icarus, 360, 114358

Campbell, B. A., Putzig, N. E., Carter, L. M., et al. 2013a, Journal of Geophysical Research: Planets, 118, 436

Campbell, B. A., Putzig, N. E., Foss, F. J., & Phillips, R. J. 2013b, IEEE Geoscience and Remote Sensing Letters, 11, 632

Castaldo, L., Alberti, G., Cirillo, G., & Orosei, R. 2013, in 2013 Signal Processing Symposium (SPS), IEEE, 1–5

Croci, R., Fois, F., Flamini, E., Mecozzi, R., & Seu, R. 2007, in 2007 4th International Workshop on, Advanced Ground Penetrating Radar, IEEE, 241–245

Croci, R., Seu, R., Flamini, E., & Russo, E. 2011, Proceedings of the IEEE, 99, 794

Dresing, N., Rodríguez-García, L., Jebaraj, I. C., et al. 2023, A&A, 674, A105, doi: 10.1051/0004-6361/202345938

Dulk, G. A., Steinberg, J. L., & Hoang, S. 1984, Astronomy and Astrophysics, 141, 30

Fokker, A. D. 1965, BAN, 18, 111

Fox, N. J., Velli, M. C., Bale, S. D., et al. 2016, SSRv, 204, 7, doi: 10.1007/s11214-015-0211-6

Gerekos, C. 2023a, SHARAD-detectable type-III burst retrieval codes in STEREO and WIND, Zenodo, doi: 10.5281/zenodo.8039055

—. 2023b, List of SHARAD type-III burst candidate based on cross-detections with STEREO and Wind, Zenodo, doi: 10.5281/zenodo.8039090

—. 2023c, Quicklook mosaic of all type-III bursts detected by SHARAD, based on cross-detections with STEREO/WAVES and Wind/WAVES, Zenodo, doi: 10.5281/zenodo.8039098

Grima, C., Kofman, W., Mouginot, J., et al. 2009, Geophysical Research Letters, 36

Gurnett, D., Morgan, D., Granroth, L., et al. 2010, Geophysical research letters, 37

Holt, J. W., Safaeinili, A., Plaut, J. J., et al. 2008, Science, 322, 1235

Jebaraj, I. C., Krasnoselskikh, V., Pulupa, M., Magdalenic, J., & Bale, S. 2023a, The Astrophysics Journal Letters, under revision, 1, doi: 1

Jebaraj, I. C., Magdalenic, J., Krasnoselskikh, V., Krupar, V., & Poedts, S. 2023b, Astronomy and Astrophysics, 670, A20, doi: 10.1051/0004-6361/202243494

Jebaraj, I. C., Kouloumvakos, A., Dresing, N., et al. 2023c, arXiv e-prints, arXiv:2301.03650, doi: 10.48550/arXiv.2301.03650

Kontar, E. P., Yu, S., Kuznetsov, A. A., et al. 2017, Nature Communications, 8, 1515, doi: 10.1038/s41467-017-01307-8

Krasnoselskikh, V., Voshchepynets, A., & Maksimovic, M. 2019, The Astrophysics Journal, 879, 51, doi: 10.3847/1538-4357/ab22bf

Krupar, V., Szabo, A., Maksimovic, M., et al. 2020, The Astrophysics Journal Supplement, 246, 57, doi: 10.3847/1538-4365/ab65bd

Kundu, M. R. 1965, Solar radio astronomy

Lecacheux, A., Steinberg, J.-L., Hoang, S., & Dulk, G. 1989, Astronomy and Astrophysics, 217, 237

Maksimovic, M., Bale, S. D., Chust, T., et al. 2020, Astronomy and Astrophysics, 642, A12, doi: 10.1051/0004-6361/201936214

Melrose, D. B. 1980, SSRv, 26, 3

Müller, D., Marsden, R. G., St. Cyr, O. C., & Gilbert, H. R. 2013, SoPh, 285, 25, doi: 10.1007/s11207-012-0085-7

Musset, S., Maksimovic, M., Kontar, E., et al. 2021, arXiv e-prints, arXiv:2109.13713. https://arxiv.org/abs/2109.13713

Picardi, G., Biccari, D., Seu, R., et al. 2004, Planetary and Space Science, 52, 149 , doi: http://doi.org/10.1016/j.pss.2003.08.020

Pulupa, M., Bale, S. D., Bonnell, J. W., et al. 2017, Journal of Geophysical Research (Space Physics), 122, 2836, doi: 10.1002/2016JA023345

Reid, H. A., & Kontar, E. P. 2018, Astronomy & Astrophysics, 614, A69

Reid, H. A. S., & Ratcliffe, H. 2014, Research in Astronomy and Astrophysics, 14, 773

Romero-Wolf, A., Vance, S., Maiwald, F., et al. 2015, Icarus, 248, 463

Seu, R., Biccari, D., Orosei, R., et al. 2004, Planetary and Space Science, 52, 157 , doi: http://doi.org/10.1016/j.pss.2003.08.024

Skolnik, M. I. 1980, New York, McGraw Hill Book Co., 1980. 590 p.

Slavney, S., & Orosei, R. 2007a, Planetary Data System (PDS)

—. 2007b, Planetary Data System (PDS)

Suzuki, S., & Dulk, G. A. 1985, in Solar Radiophysics: Studies of Emission from the Sun at Metre Wavelengths, ed. D. J. McLean & N. R. Labrum (Cambridge University Press), 289–332

Tkachenko, A., Krasnoselskikh, V., & Voshchepynets, A. 2021, The Astrophysics Journal, 908, 126, doi: 10.3847/1538-4357/abd2bd

Van Haarlem, M. P., Wise, M. W., Gunst, A. W., et al. 2013, Astronomy and Astrophysics, 556, A2, doi: 10.1051/0004-6361/201220873

Voshchepynets, A., & Krasnoselskikh, V. 2015, Journal of Geophysical Research (Space Physics), 120, 10,139, doi: 10.1002/2015JA021705

Voshchepynets, A., Krasnoselskikh, V., Artemyev, A., & Volokitin, A. 2015, The Astrophysics Journal, 807, 38, doi: 10.1088/0004-637X/807/1/38